AGU ADVANCING EARTH AND SPACE SCIENCE

Earth and Space Science

RESEARCH ARTICLE
10.1029/2023EA002903

Key Points:

- We present infrared spectra of basaltic samples from the Bühl, Hesse, Germany in preparation of the MERTIS experiment
- Comparison of feldspars formed at different oxygen fugacities showed no spectral differences
- This is an important result for MERTIS, which will investigate Mercury that formed under reducing conditions

Correspondence to:
M. P. Reitze,
maximilian.p-reitze@uni-muenster.de

Citation:
Reitze, M. P., Weber, I., Morlok, A., Hiesinger, H., Pasckert, J. H., Schmedemann, N., et al. (2023). Mid-infrared spectroscopy of feldspars from the Bühl basalt (Northern Hesse, Germany) formed under reducing conditions as terrestrial analogue of Mercury for MERTIS. *Earth and Space Science*, *10*, e2023EA002903. https://doi.org/10.1029/2023EA002903

Received 23 FEB 2023
Accepted 15 MAY 2023

Author Contributions:
Conceptualization: Maximilian P. Reitze
Formal analysis: Maximilian P. Reitze
Investigation: Maximilian P. Reitze
Methodology: Maximilian P. Reitze
Supervision: Harald Hiesinger, Jörn Helbert
Validation: Maximilian P. Reitze
Visualization: Maximilian P. Reitze
Writing – original draft: Maximilian P. Reitze
Writing – review & editing: Iris Weber, Andreas Morlok, Harald Hiesinger, Jan Hendrik Pasckert, Nico Schmedemann, Karin E. Bauch, Aleksandra N. Stojic

Mid-Infrared Spectroscopy of Feldspars From the Bühl Basalt (Northern Hesse, Germany) Formed Under Reducing Conditions as Terrestrial Analogue of Mercury for MERTIS

Maximilian P. Reitze[1], Iris Weber[1], Andreas Morlok[1], Harald Hiesinger[1], Jan Hendrik Pasckert[1], Nico Schmedemann[1], Karin E. Bauch[1], Aleksandra N. Stojic[1], and Jörn Helbert[2]

[1]Westfälische Wilhelms-Universität Münster, Institut für Planetologie, Münster, Germany, [2]Deutsches Zentrum für Luft- und Raumfahrt (DLR), Berlin, Germany

Abstract The MErcury Radiometer and Thermal Infrared Spectrometer instrument onboard the BepiColombo spacecraft is designed to investigate Mercury's surface in the mid-infrared (mid-IR). Based on MESSENGER data and modeling, Mercury is thought to be evolved under highly reducing conditions (e.g., McCubbin et al., 2017, https://doi.org/10.1002/2017JE005367; Namur & Charlier, 2017, https://doi.org/10.1038/ngeo2860). The modeling also indicates that Mercury's surface is rich in feldspar. However, it is unknown if reducing conditions during the emplacement of volcanic melts have an influence on the IR properties of feldspars. Therefore, we investigated basaltic samples from the Bühl quarry in northern Hesse, Germany, that evolved under reducing conditions in the mid-IR and compared the spectra with samples that experienced more oxidizing conditions during their formation. The Bühl samples are feldspar-rich and contain metallic iron in some areas. Our investigations show that there are no differences between feldspars that formed under different oxidizing conditions. All spectral properties could be explained by well-known factors that affect mid-IR spectra of silicates.

Plain Language Summary ESA's and Japan Aerospace Exploration Agency's spacecraft BepiColombo is equipped, beside other instruments, with a thermal infrared (IR) radiometer and spectrometer called MErcury Radiometer and Thermal Infrared Spectrometer (MERTIS). For the accurate interpretation of the data from the MERTIS instrument, laboratory analog material is necessary. This analog material must fulfill different characteristics, such as different chemical and mineralogical compositions. Another not yet studied property is the availability of oxygen during the formation of the minerals. Depending on how much oxygen is available, different minerals form. However, this is an important feature, because Mercury is thought to have evolved under highly reducing conditions, as opposed to Earth where nearly all material formed significant more oxidizing conditions. One phase that is strongly associated with reducing magma formation conditions is metallic iron. There are only few natural outcrops on Earth, were stronger reducing conditions were present so that metallic iron could be formed. One of these outcrops is the Bühl quarry in northern Hesse, Germany. From there we used different samples to analyze the effect of oxygen availability on mid-IR spectra of plagioclase feldspars.

1. Introduction

Mercury is the innermost planet in our Solar System and the target of the BepiColombo spacecraft, which is equipped with the thermal infrared (IR) spectrometer and radiometer MErcury Radiometer and Thermal Infrared Spectrometer (MERTIS), besides other instruments (Benkhoff et al., 2010; Hiesinger et al., 2010, 2020). The spectrometer of MERTIS has 78 spectral channels in the wavelength range between 7 and 14 μm (Hiesinger et al., 2010, 2020). The footprint of the measurements on Mercury will globally reached 500 m × 500 m and better than this at up to 10% of the surface (Hiesinger et al., 2020). The goals of MERTIS are (a) studying Mercury's surface composition, (b) identifying of rock-forming minerals, (c) mapping the surface mineralogy, and (d) studying the thermal inertia (Hiesinger et al., 2010, 2020). To achieve the goals of MERTIS, it is necessary to build a spectral library of fully characterized samples of potential constitute minerals of Mercurys' surface and to study the behavior of mixtures of these minerals (Weber et al., 2018). Analog experiments and modal calculations with chemical compositions derived from MESSENGER data were performed (e.g., Morlok et al., 2021; Namur & Charlier, 2017) to identify potential mineral candidates.

In contrast to Earth, Mercury evolved under strong reducing conditions well below the iron-wüstite bufffer (McCubbin et al., 2017; Namur et al., 2016). Hence, because formation conditions of magmatic rocks on Earth were stable oxidizing over time (Anser Li & Aeolus Lee, 2004), terrestrial analog material mostly developed under conditions different from those on Mercury (e.g., Papike et al., 2004). However, there are only three known examples on the Disko Island on Greenland, a large outcrop in the Siberian traps, and one in the middle of Germany at the Bühl near Kassel in northern (also called lower) Hesse (e.g., Pernet-Fisher et al., 2017), where strong reducing conditions (fO_2-fugacites below iron-wüstite buffer) during the emplacement of the rocks wereat least partially prevalent. All those deposits were formed at the contact zone between volcanic melts and coal deposits (e.g., Medenbach & El Goresy, 1982; Ryabov & Lapkovsky, 2010). Model calculations show that for the reduction process comparatively small amounts of organic matter are necessary (Iacono-Marziano et al., 2012). Metallic iron is found as end product of a reduction process in all three localities in those areas where the oxygen fugacity was below the iron-wüstite buffer. Therefore, the occurrence of metallic iron is unique on Earth and has not been found elsewhere within terrestrial rocks. Only some meteorites display these similar special reducing conditions (e.g., Anders, 1964).

The "Bühl" itself is a flooded quarry of a former volcanic cone with an approximate diameter of around 150 m located at N51°21′25.67″, E9°23′6.99″ in Ahnatal-Weimar north-west of Kassel. The northern Hesse basalt province is located in the northern extension of the Rheingraben and the Vogelsberg basalt complex (e.g., Brey, 1978). In the very first description of the Bühl in 1867, the basaltic cone was already 10–21 m above the ground level although the mining started in 1843 and no metallic iron was reported indicating that the iron deposites and therefore the reducing conditions are located in deeper layers of the cone (Möhl, 1868). The first found of metallic iron in the Bühl was reported by Hornstein (1907). Siderite and limonite in the brown coal deposited between the middle Eocene to the early Oligocene (48–28 Ma BP) around the Bühl were incorporated intosome parts of the magma eruption in the Miocene (20–7 Ma) (Karl, 2021; Ramdohr, 1953). The siderite and limonite fragments were reduced to metallic iron by the presence of the brown coal that served as the reducing agent (Ramdohr, 1953). In the area of the cones rim, silicate fragments from the cross-cuted sediment layers were also found (Velde, 1920). Even though in the region in northern Hesse around the Bühl numerous basaltic deposits are located, which also cross-cut the Eocene and Oligocene sediments, the Bühl is the only deposit from which metallic iron is known (e.g., Blanckenhorn & Beyschlag, 1901; Irmer, 1920). The occurrence of metallic iron and ulvöspinell in the basalts made samples from the Bühl ideal analog material of the Moon's mare basalts (e.g., Ballhaus et al., 2022; El Goresy et al., 1971).

In 2020, the BepiColombo spacecraft performed a flyby at the Earth-Moon system to bring the satellite on a trajectory into the inner Solar System (e.g., Hiesinger et al., 2021). During this flyby, the MERTIS instrument was able to observe the surface of the Moon as the firsthyperspectral spacecraft-based instrument in this wavelength region between 7 and 14 μm (Hiesinger et al., 2021). Before, DIVINER measured with three broad channels between 7.55 and 8.68 μm (Paige et al., 2010). For the correct interpretation of these data, it is necessary to know and identify the aspects that influence IR spectra of the different minerals of the lunar surface. The question arises whether minerals, for example, feldspars, exhibit different spectral signatures due to the conditions under which they formed because it is known that the oxygen fugacity has an influence on the crystallization temperature of minerals in combination with high pressures (e.g., D. L. Hamilton et al., 1964). This might have an effect on the crystal structure or the degree of Al,Si order. To answer this questionwhether or not the oxygen fugacity has an effect on the mid-IR spectra, a detailed spectral analysis of the different phases within the complex samples and their respective spectra is necessary. In particular, mid-IR spectra of silicate minerals and rocks show distinct spectral features, which can be analyzed in terms of band position (wavelength or wavenumber) and band shape. These features are (a) the Christiansen Feature (CF), which is a chemical composition-related global minimum in reflectance spectra (or maximum in emission spectra), (b) the Reststrahlen bands (RBs), which are the result of silicon and oxygen bonding modes, and (c) in spectra of fine-grained powders the Transparency Feature (TF), which occurs due to the change from surface-scattering at the larger grains to volume-scattering in the smaller grains (e.g., Pieters & Englert, 1993).

The Bühl samples can be used not only as terrestrial analog material for the Moon, but also for Mercury to interpret spectroscopic observations performed by MERTIS during its nominal mission. The samples are particularly important for Mercury observations by MERTIS, which will begin after BepiColombo arrives at its Mercury mapping orbit in 2026. Although Mercury's surface is strongly depleted in iron (Namur & Charlier, 2017), it is, based on Earth-based spectroscopic observations, assumed to be rich in feldspar (e.g., Donaldson Hanna

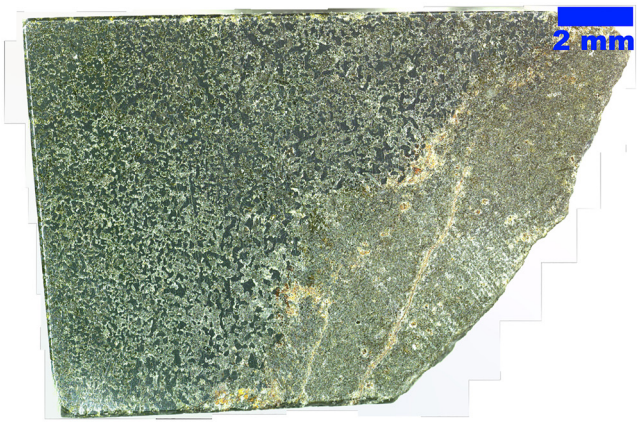

Figure 1. Reflected light image of ID 500 acquired with Keyence Digital Light Microscope VHX-500F. The sample consists mainly of metallic iron (dark-gray) at the left-hand site and silicate material on the right-hand site.

et al., 2007; Sprague et al., 1994, 1997, 2002, 2007, 2009). Therefore, the minerals in the close proximity of the metallic iron within the Bühl-samples are a good terrestrial analog material because these minerals were also exposed to reducing conditions during their formation. With the IR microscope it is possible to measure only the minerals in the close proximity of the iron without simultaneously measuring the metallic iron. Because both, the Bühl samples that experienced reducing conditions and the Bühl samples that experienced more oxidizing conditions contain mostly of plagioclase, the question can be answered whether reducing conditions have an influence on the spectral behavior of the feldspar spectra. This is the first study that investigates probable changes of mid-IR spectra due to the redox conditions during the crystallization of the magma, to our knowledge.

2. Samples and Analyses

The Bühl basalt was analyzed by different authors (e.g., Irmer, 1920, and references therein). Irmer (1920) divided the basalts into four groups depending on their occurrence according to the terms used by the pit workers: (a) in the north and east the "ordinary basalt," (b) in the southeast the "soft basalt," (c) in the southwest "massive basalt," and (d) in the northwest the "hard or fine-grained basalt." Iron was first found in lower abundances in the ordinary basalt in rounded segregates and higher abundant in deeper layers of the hard basalt as separate phase (Irmer, 1920).

Ramdohr (1953, the text is only available in German; therefore, we give a short summary here) gave a detailed petrographic description although the quarry was flooded already partially in 1920. Ramdohr (1953) subdivided the iron in the Bühl basalts into two groups. The first group consists of Fe in form of nodules with sizes often larger than 8 cm in diameter. These are surrounded by a very iron-poor silicate-rich rim, which is about 0.5 cm thick including droplets of iron. The second group consists of iron that shows a sponge-like intergrowth with the silicate matrix.

Besides iron, the samples consist of large amounts of plagioclase, magnetite, pyrrhotite, ilmenite, hematite, ulvöspinell, cohenite, and magnesioferrite (Ramdohr, 1953). Ramdohr (1953) did not mention olivine, however, Irmer (1920), Velde (1920), and Medenbach and El Goresy (1982) identified olivine within the iron bearing xenoliths. Köster (1953) described also molybdenite in samples of the Bühl.

For this study, we used two different samples of the Bühl basalt. The first is a cubic block of approx. 1.5 cm ×1 cm ×1 cm edge length, consisting mostly of iron and less basaltic melt and represents a sample which formed under reducing conditions (Figure 1). This historical sample was also used by Ramdohr and was superficially corroded. Ramdohr (1953) reported that the iron is always uncorroded and fresh in his samples. Therefore, the corrosion of our sample was likely an effect of the long storage time under unfavorable conditions and therefore not genetic. For our analyzes, we carefully removed the corrosion crust by polishing. The sample identification number (ID) is 500, which will be used in the following.

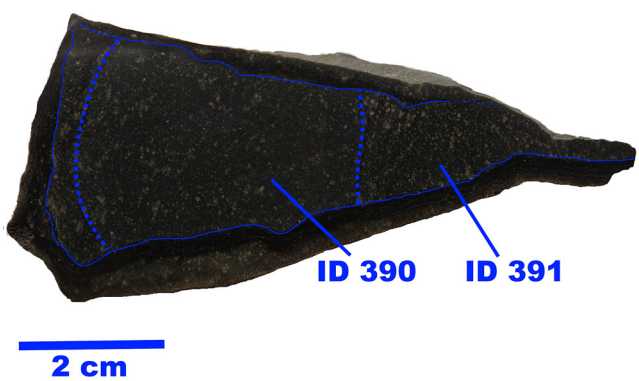

Figure 2. Hand piece of ID 385. A dark/black rim surrounds two lithologies in the center. The left one (ID 390) appears darker, the right one (ID 391) lighter. Below the darker phase, some of the lighter phase seems to be present indicating that the lighter phase surrounds the darker at least in some parts.

The second sample was recently collected at the Bühl in the northern part from the mining waste material in the upper part of the pit (Figure 2). The collected specimen was around 7 cm ×5 cm ×5 cm large with a relative round occurrence and is labeled with ID 385 from here on. The sample is weakly attracted by a strong magnetic field. A thin section was prepared from this sample (Figure 3). Three different lithologies can be distinguished within the specimen. An approx. 0.1–0.5 cm thick rim appears black in the polished specimen and brownish in the thin section. At the outer rim of the hand piece, this dark rim appears rusty brown-red indicating oxidation of Fe-containing material. There is no metallic iron within this sample, which shows that it experienced more oxidizing conditions during its formation

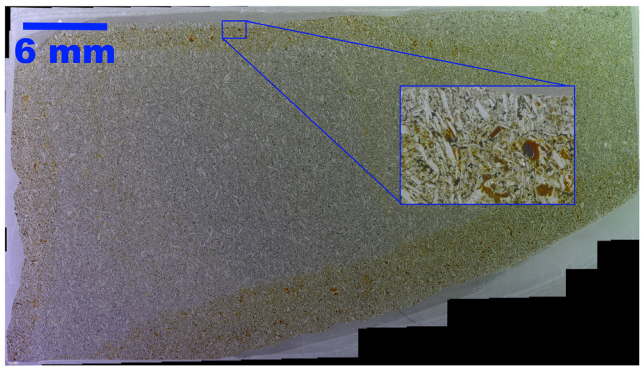

Figure 3. Image of ID 385 thin section acquired with Keyence Digital Light Microscope VHX-500F. A brownish rim surrounds two phases, whereas one at the left is the darker phase in the hand piece and the light brownish phase appears lighter in the hand piece. The inserted square (dimensions approx. 2.7 mm × 1.2 mm) marks the region of FTIR-Microscope measurements on the rim (compare Figure 4).

than ID 500. This rim encloses two different areas. A darker lithology, around 2 cm × 2 cm in size and a brighter phase which seems to partially surround the darker lithology. The two lithologies in the interior have a well-defined border. We prepared powders with a steel pestle and mortar by hand from the two lithologies to additionally produce regolith analog material. The sample prepared from the darker lithology has ID 390 and the sample prepared from the brighter lithology has ID 391. The powders were sieved into grain size fractions from smaller than 25, 25–63, 63–125, and 125–250 µm. The analysis of grain size separates are necessary, because the mechanical behavior of the minerals is different leading to changes of mineral abundances within the different grain size fractions (e.g., Reitze et al., 2021a). This effect is observed in the Moon's regolith and therefore expected on Mercury Taylor et al. (2001).

All IR spectra are stored in the IRIS IR database, see the "Data Availability Statement" for details.

2.1. Sample Characterization

We investigated the samples with an optical light microscope (transmitted and/or reflected light) to search for regions of interest (ROI) and to determine the mineralogy. Electron microprobe analysis were conducted with a JEOL JXA-8530F at the institute for mineralogy, WWU, Münster, Germany, to characterize the chemical composition of all present minerals with a spot size of 1 µm in samples ID 385. Sample ID 500 is to large for the electron microprobe but should not be destroyed because of its rareness. Therefore, we used a raster electron microscope JEOL 6610-LV in low vacuum mode with 20 kV acceleration voltage to confirm the findings of Irmer (1920). The chemical composition analysis are given in Table 2. IR analyses were performed with two different spectrometers. We used a Bruker VERTEX 70v equipped with a liquid nitrogen (LN_2) cooled MCT-detector to investigate the powder samples at 2 hPa and room temperature (RT ≈ 23°C) in forward-backward mode with 512 scans per sample using a variable, biconical reflectance accessory (A513) with an incidence angle of 20° (i20°) and an emergent angle of 30° (e30°). The powder samples itself were filled in aluminum cups, which were first overfilled and then flattened with a spatula to reach a planar surface. A commercial rough gold mirror INFRAGOLD™ served as background, which was measures prior to the samples under the same conditions with the same instrument settings.

The thin section of ID 385 and the block samples ID 500 were analyzed with a Bruker Hyperion 3000 IR microscope coupled to a Bruker VERTEX 80v. All microscope measurements were performed under ambient pressure and at RT. The IR microscope was purged with dry air to stabilize the atmospheric bands and mostly remove them from the spectra. We used a polished gold mirror as background for the microscope measurements. The illumination angle and emergent angle of the IR light are both 0° in the FTIR microscope. The measurements with the IR microscope were performed with the LN_2 cooled single element MCT-detector and an adjustable knife-edge aperture to select the ROI. All measurements in both devices were performed with a spectral resolution of 4 cm^{-1}, which leads to a spectral resolution that is comparable to that of the MERTIS instrument operating in the spectral range between 7 and 14 µm (Hiesinger et al., 2010, 2020).

3. Results

We present the results for varying grain size separates and phase analyses for each sample. Table 1 gives a summary of the identified wavelength positions in the text. Table 2 gives the results of electron microprobe and EDX analysis of the samples.

3.1. Thin Section Sample ID 385

Light microscopic examinations of the samples show a uniform in grain size distribution within the three different lithologies (Figure 3). All three lithologies are dominated by feldspar. The different colors of the lithologies result from the presence of darker phases, which are brown in the thin section. We concentrated on the feldspars,

Table 1
Wavelength in Micrometer of the Christiansen Features and Reststrahlen Bands for All Samples and Their Respective Grain Sizes or Phases Measured With the Infrared Microscope and VERTEX 70v

ID	Phase/Grainsize	CF	RB_1	RB_2	RB_3	RB_4	TF_1	TF_2	Potential mineral
385	Plagioclase (1)	8.00*	8.97	10.03					Plagioclase An_{50-70}
	Plagioclase (2)	7.97*	8.93	10.09					Plagioclase An_{50-70}
	black-gray (3)	8.58	9.73						Phyllosilicate Siderophyllite
	gray (4)	8.21*	9.78						Phyllosilicate Chlorite
	black-white (5)	8.59	9.68						Phyllosilicate
	White 1 (6)	8.10	9.11	10.01					Phyllosilicate (?) dominated by plagioclase
390	63–125 µm	7.98	9.14	9.88					
	25–63 µm	8.00	9.10	9.88					
	<25 µm	8.11	9.01	9.90	10.55		12.11	11.37	
391	63–125 µm	7.93	9.12	9.85					
	25–63 µm	8.02	9.12	9.92					
	<25 µm	8.12	9.12	9.94	10.62		12.11	11.43	
500	Pyroxene	7.83*	9.02	10.01	10.41	10.92			Pyroxene
	Plagioclase (Px1)	8.00	8.96	10.05	10.54				Plagioclase
	Plagioclase (Px3)	8.03	8.94	10.07					Plagioclase

Note. Numbers in brackets refer to the text. The most intense TF is marked with index 1, shoulders or smaller features related with the TF are marked with index 2. The asterisk marks CFs, which are uncertain. Wavelength in micrometer. Reference spectra for plagioclase see Reitze et al. (2021b), for phyllosilicates see the USGS spectral database (Kokaly et al., 2017), for example, siderophyllite NMNH104998 and chlorite HS197.3B, for pyroxene and plagioclase dominated rock spectra Reitze et al. (2021a).

however, all minerals/phases comprising the sample were measured thoroughly with the IR microscope to give a complete spectral overview of ID 385. The spectra of the individual unspecified phases are named after their color appearance in the FTIR microscope VIS-monochrome image. The inset in Figure 3 shows the region on the rim, which was analyzed with the FTIR microscope in detail. Figure 4 shows the same as the inset in Figure 3 but in monochromatic light (VIS) as seen with the IR microscope. This kind of visualization shows the distinction between several phases that otherwise only appear brown in the reflected light image.

The lowest reflectance value of the microscope spectra is not necessarily the CF because, the spectra of the thin section samples sometimes show sinusoidal artifacts in the region of the shorter wavelengths below the CF. This occurs due to the highly reflective surface of the thin section, which reflects some of the IR radiation back to the interferometer where a second modulation of the radiation happens. This sometimes makes the identification of the exact wavelength of the CF challenging.

In the following, we describe the single spectra of the different phases with their color occurrence in reflected light as well as in the VIS-monochrome FTIR microscope image (compare Figure 3, as well as Figures 4–7) and their corresponding IR spectra (compare Figures 8–10; see Table 1 for a summary of band positions.). The phases/minerals are arbitrarily numbered for the readability of the text, with the label the spectra can be found in the IRIS database. (a) The phase label is plagioclase and is together with the following spectrum representative for the plagioclases in the sample (Figure 5a, measurement date for database entry 03/05/2022) Its spectrum shows a CF at 8.00 µm (1,250 cm^{-1}) and two clear RBs at 8.97 µm (1,115 cm^{-1}) and 10.03 µm (997 cm^{-1}) as well as a shoulder around 10.5 µm (952 cm^{-1}). (b) The phase is labeled as plagioclase (Figure 5 b, measurement data for database entry 10/06/2022). Its spectrum has a CF at 7.97 µm (1,255 cm^{-1}) and two RBs at 8.93 µm (1,120 cm^{-1}) and 10.09 µm (991 cm^{-1}), as well as a shoulder around 10.5 µm (952 cm^{-1}). (c) The phase with label "Black-Gray Phase" shows a brownish tinge in reflected light, but appears distinct bordered in black-gray in the monochromatic image. Its spectrum shows a CF at 8.58 µm (1,165 cm^{-1}) and one sharp peak at 9.73 µm (1,028 cm^{-1}). (d) The phase is brownish in reflected light and gray in the FTIR microscope image. Its spectrum has a CF at 8.21 µm (1,219 cm^{-1}). However, the CF is more difficult to identify because of the described

Earth and Space Science

10.1029/2023EA002903

Table 2
Oxide Wight-Percent for ID 385 Measured With an Electron Microprobe and for ID 500 Measured in Low-Vacuum Mode With a REM

ID 385	"Andesine"	"Labradorite"	"Pyroxen" low Ca	"Pyroxen" high Ca
Na_2O	6.0 (0.2)	5.1 (0.3)	0.10	0.20
MgO	0.10 (0.02)	0.14 (0.02)	21.07	16.10
Al_2O_3	26.0 (0.4)	27.3 (0.4)	0.6	1.39
SiO_2	56.7 (0.5)	54.8 (0.6)	52.59	51.27
K2O	0.25 (0.04)	0.15 (0.04)	0.00	0.02
CaO	9.4 (0.5)	11.1 (0.4)	4.45	14.01
FeO	0.69 (0.07)	0.5 (0.1)	19.43	14.63
TiO_2	0.14 (0.05)	0.09 (0.03)	0.47	1.08
Cr_2O_3	0.02 (0.02)	0.01 (0.01)	0.16	0.06
MnO	0.01 (0.01)	0.01 (0.01)	0.42	0.33
NiO	0.01 (0.01)	0.02 (0.02)	0.08	0.05
Total	99.27	99.23	99.34	99.13
	Ab 46	Ab 54	En 60	En 47
	An 53	An 45	Wo 9	Fs 29
	Or 1	Or 1	Fs 31	Wo 24

ID 500	"Labradorite"	"Pyroxene"
Na_2O	6.0 (0.4)	0.9 (0.4)
MgO	0.8 (0.2)	23 (9)
Al_2O_3	24.7 (0.8)	4 (1)
SiO_2	55.2 (0.3)	51 (6)
P_2O_5	0.11 (0.07)	0.04 (0.07)
SO_3	0.1 (0.1)	0.1 (0.1)
K_2O	0.29 (0.07)	0.16 (0.04)
CaO	8.1 (0.9)	4 (2)
TiO_2	0.4 (0.1)	0.6 (0.3)
Cr_2O_3	0.05 (0.02)	0.1 (0.1)
MnO	0.19 (0.07)	0.5 (0.1)
FeO	4.1 (0.9)	16 (1)
NiO	0.04 (0.04)	0.01 (0.07)
Total	100.00	100.00
	Ab 24	En 52
	An 73	Wo 12
	Or 3	Fs 36

Note. Results are mean values, expect for the ID 385 pyroxens which indicate the lowest and highest Wo-values to show the range of zoning. Numbers in brackets indicate the standard deviation.

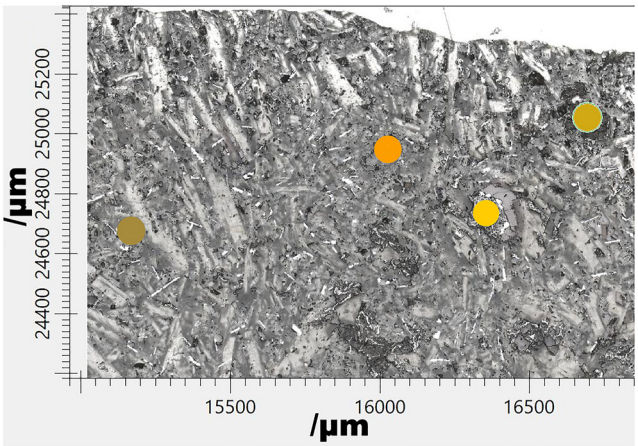

Figure 4. ID 385: The inset from Figure 3 as seen with the FTIR microscope in reflected light (VIS-monochrome). The feldspar laths show different gray colors. Phases that appear brownish in the thin section occur black to dark gray. Color-coded measuring spots refer to alteration phases (see Figure 8). The knife-edge aperture is always smaller than the colored points.

artifact at the short-wavelength end of the spectrum. The spectrum has a sharp peak at 9.78 µm (1,022 cm^{-1}). At the longer wavelength side of the sharp peak, three shoulders appear. This phase was named "Gray Phase." (e) The phase appears black in reflected light and black-white patterned in the monochromatic image. Its spectrum has a CF at 8.59 µm (1,165 cm^{-1}) and a sharp peak at 9.68 µm (1,034 cm^{-1}). The peak is asymmetric with underlying shoulders at the long wavelength side of the peak. Its name is Black-White Phase 1. (f) The phase labeled White Phase 1 and its spectrum has a CF at 8.10 µm (1,234 cm^{-1}) and RB peaks at 9.11 µm (1,097 cm^{-1}) and 10.01 µm (999 cm^{-1}).

3.2. Powder Samples ID 390 and ID 391

The plagioclase components dominate the IR spectral bands of the bulk powders (Table 1). This is indicated, for example, by the wavelength (wavenumber) of the CF. The spectrum of the sample ID 390 with the grain size between 63 and 125 µm shows a CF at around 7.98 µm (1,253 cm^{-1}) and the sample ID 391 with the same grain size at 7.93 µm (1,261 cm^{-1}), respectively. Both samples show two clear RBs in the spectra of the 63–125 µm grain size separates at 9.14 µm (1,094 cm^{-1}) and at 9.88 µm (1,013 cm^{-1}) in ID 390 and at 9.12 µm (1,096 cm^{-1}) and 9.85 µm (1,015 cm^{-1}) in ID 391.

The grain size separates from 25 to 63 µm show a CF at 8.00 µm (1,251 cm^{-1}) in the spectrum of ID 390 and at 8.02 µm (1,246 cm^{-1}) in the spectrum of ID 391. Both spectra of the grain size separates from 25 to 63 µm show two clear RBs. The spectrum of ID 390 shows the first RB at 9.10 µm (1,098 cm^{-1}) and the second at 9.88 µm (1,013 cm^{-1}). The spectrum of ID 391 with the same grain sizes shows the first RB at 9.12 µm (1,096 cm^{-1}) and the second at 9.92 µm (1,008 cm^{-1}).

The spectra of the smallest grain size fraction of ID 390 and ID 391 show the CF at 8.11 µm (1,236 cm^{-1}) and 8.12 µm (1,234 cm^{-1}), respectively. The RBs in the spectra are located at 9.12 µm (1,096 cm^{-1}) for both samples ID 390 and ID 391 and at 9.92 µm (1,008 cm^{-1}) in ID 390 and 9.94 µm (1,006 cm^{-1}) in ID 391. The TF in the spectra of the fine-grained fractions of the samples ID 390 and ID 391 show a relatively sharp TF at 12.11 µm (826 cm^{-1}) and a less intense band at 11.37 µm (880 cm^{-1}) in ID 390 and at 11.43 µm (875 cm^{-1}) in ID 391.

3.3. Block Sample ID 500

The sample consists of two parts, one more iron-rich and one more silicate-rich area (Figure 1). The iron shows a sponge-like distribution/intergrowth. Therefore, it can be classified into the second group of iron occurrences in the Bühl basalt described by Ramdohr (1953).

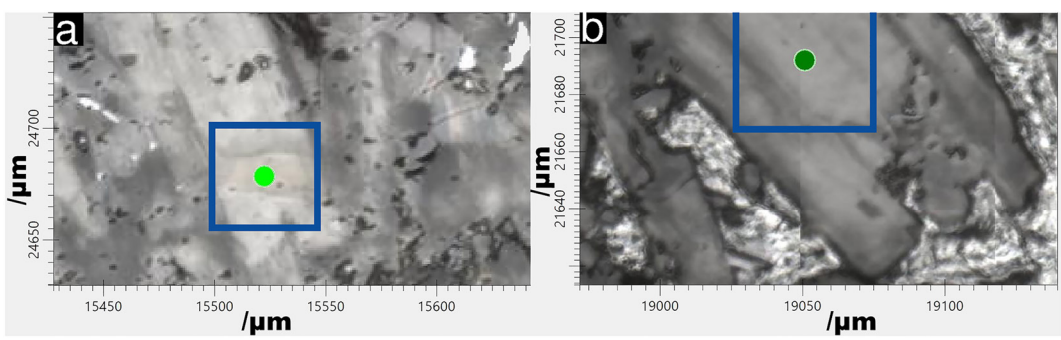

Figure 5. FTIR-Microscope (VIS-monochrome) images of plagioclase measurement areas on the thin section of ID 385 with an approx. size of the knife edge aperture (blue boxin (a) 45 × 60 $µm^2$, in (b) 30 × 30 $µm^2$). Measurement spots are color-coded, compare Figure 11.

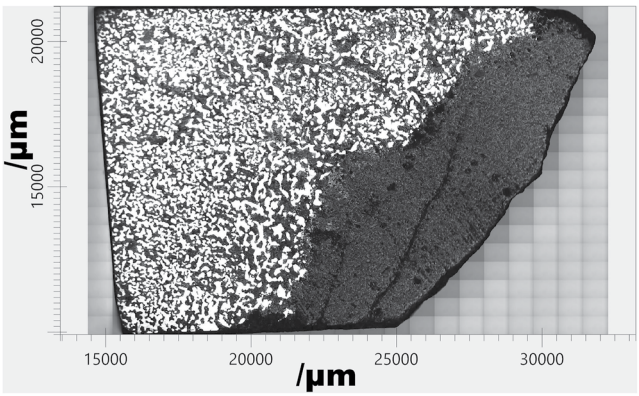

Figure 6. FTIR-Microscope (VIS-monochrome) overview of ID 500. Bright white phase is metallic iron, black to gray colored phases are silicates.

The crystals are larger than in ID 385. We measured the phases visible in the monochromatic optical FTIR-microscope image (Figure 6). The silicate phases in the immediate neighborhood of the iron droplets were of particular interest, as they experienced the same reducing environment as the metallic iron did. In these images the iron occurs bright-white with some visible scratches from sample polishing. Other mineral phases are dark-gray to black and difficult to distinguish from each other.

Iron shows a relatively high and uniform reflectance. Spectral bands visible in the "pure" iron spectrum are related to small silicate accessories (Stojic et al., 2021). The spectrum that is taken with an aperture covering an iron + silicate mix also shows the flat iron spectrum with superposed silicate bands. The spectrum of the darker phase has its lowest reflectance value at 7.83 µm (1,277 cm^{-1}). However, this value might not reflect the CF because the spectrum is noisy in this spectral range. Furthermore, the spectrum shows four clear RBs at 9.02 µm (1,109 cm^{-1}), 10.01 µm (999 cm^{-1}), 10.41 µm (960 cm^{-1}), and at 10.92 µm (916 cm^{-1}). We identified the phase as magnesium-rich pyroxenebased on the RB although the position of the CF is unexpected for these pyroxenes, most likely because of the noisy spectrum (e.g., V. E. Hamilton, 2000). The two spectra with CF around 8.00 µm (1,250 cm^{-1}; Pixel index 1) and 8.03 µm (1,245 cm^{-1}; Pixel index 3) are clearly plagioclase feldspars. Both show comparable RB peaks around 8.95 µm (1,117 cm^{-1}; Pixel index 1) and 10.06 µm (994 cm^{-1}; Pixel index 3). One exhibits a third clear RB at 10.54 µm (949 cm^{-1}; Pixel index 1) where the other (Pixel index 3) spectrum shows a shoulder in this region. Both plagioclase spectra were taken in the direct vicinity of an iron droplet (Figure 7).

4. Discussion

We investigated two different basaltic samples from the Bühl quarry near Kassel, Germany, in the mid-IR to investigate possible spectral changes that occur due to different reducing conditions (oxygen fugacities). Before we discuss the spectral behavior of the samples that originate from different reducing condition environments, we have to summarize well-known factors that influence the sample spectra. One important factor used in the literature relevant for the discussion of the samples from this study is their grain size (e.g., Lyon, 1964; Pieters & Englert, 1993; Shirley & Glotch, 2019). The spectral behavior of granular material comprised of larger grain sizes show more similarity to the spectral behavior of solid samples (e.g., Salisbury & Wald, 1992). For example, granular samples with a grain size below approximately 74 µm start to show a TF in their spectra, which becomes increasingly prominent with deceasing grain size (Salisbury & Walter, 1989). However, even the smallest constituents of thin sections analyzed with an IR microscope will not show a TF, due to the presence as a closed surface without porosity. In addition, compacting a powder sample leads to a decreased TF (Hapke & Sato, 2016; Salisbury & Eastes, 1985; Weber et al., 2020). This shows, that the porosity of the sample, which can be correlated with the grain size but more strongly with the sample preparation, is an important underlying

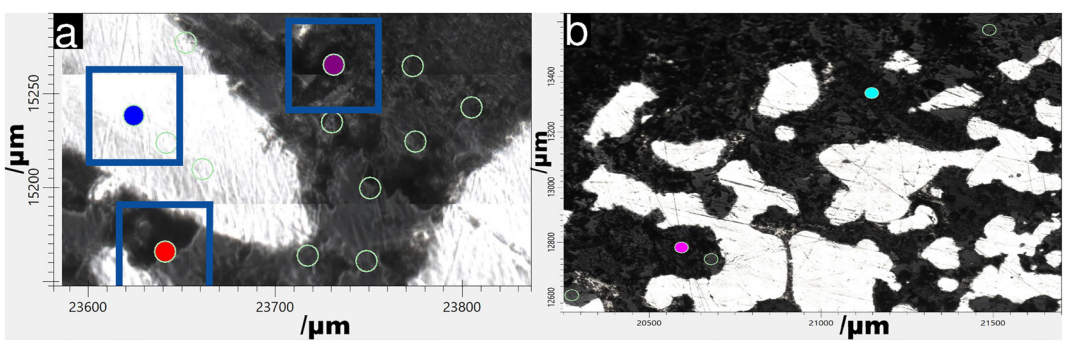

Figure 7. FTIR-Microscope (VIS-monochrome) images of measured areas on thin section ID 500 (approx. size of the knife edge aperture (a) blue box: 50 × 50 $µm^2$; (b) 20 × 20 $µm^2$, smaller than the dots). Measurement spots are color-coded, compare Figures 10 and 11.

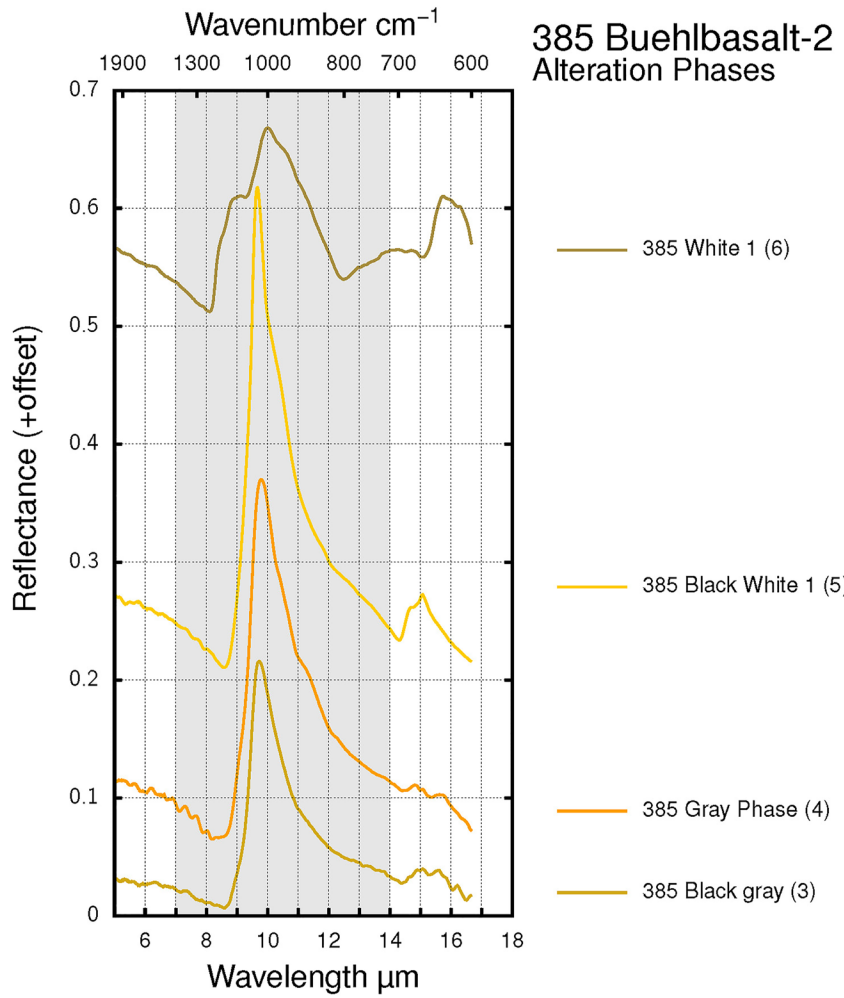

Figure 8. Alteration phases of ID 385 measured with the FTIR-microscope (see Figure 4). The phases are phyllosilicates with varying composition indicated by a shift of the strong Reststrahlen band and a shift of the Christiansen Feature. Numbers in round brackets refer to the text.

factor that affects the spectral behavior, most importantly the TF (Salisbury & Eastes, 1985; Weber et al., 2020). However, in order to compare our results to those in the literature, we use the grain size to classify the spectra. In addition, spectra of powdered samples are dominated by diffuse reflection while microscope spectra of polished samples show a stronger specular reflection (Kortüm, 1969). However, the wavelength of specific features is not affected by this.

For IR microscope measurements, the crystal orientation can have an effect on the spectra (e.g., Jaret et al., 2015). Therefore, we analyzed IR microscope spectra, which do not show orientation effects, because the regolith grains of atmosphereless planetary bodies are randomly orientated. However, during sample preparation, it must kept in mind that any compacting of powdered sample may lead to the orientation of the crystals. Therefore, we overfill our powder sample holders and than only carefully flatten the samples with a spatula once to remove and flat the samples surface to avoid alignment of the crystals.

With this sample preparation technique, we also mostly avoid a compaction of the samples. The analyzed samples in this study are iron-dominated (ID 500) and without metallic iron consisting mainly of plagioclase (ID 385). Sample ID 385 and its sub-samples ID 390 and ID 391 contain phyllosilicates originating from aqueous alteration (Figure 8). Spectroscopically the altered mineral phases are well distinguishable from un-altered or fresh phases with the IR microscope. In addition, the alteration products do not significantly influence the spectra of the powder samples of ID 390 and ID 391 (Figure 9). The plagioclases of ID 385 have mainly two different chemical

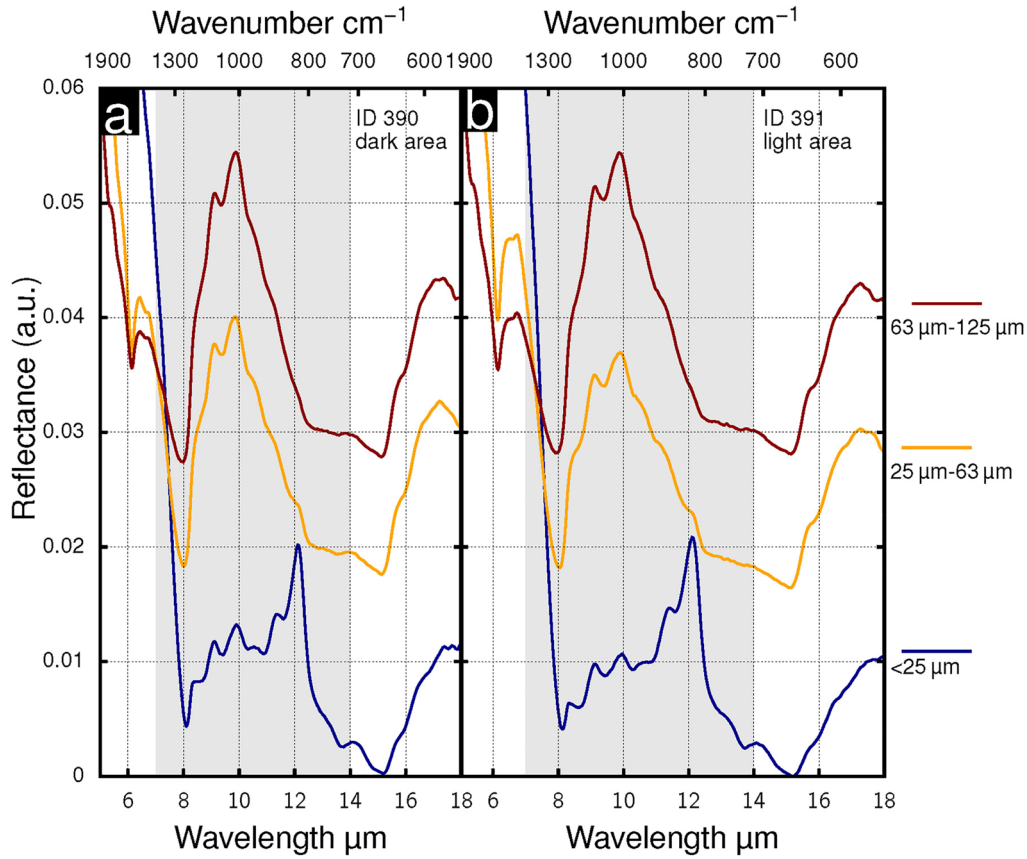

Figure 9. Spectra of the (a) IDs 390 and 391 (b), which were prepared from ID 385. Whereas the two areas are clearly distinguishable in the VIS, there are no spectral differences visible in the MIR.

compositions, possibly due to fractional crystallization. One is more An-rich ("Labradorite") with a mean of $An_{54}Ab_{45}Or_1$ (15 analyses) and the other more Ab-rich ("Andesine") with $An_{46}Ab_{53}Or_1$ (12 analyses). These values differ from the findings by Irmer (1920), who described the whole range of chemical compositions of the plagioclases as "labradoritic close to the bytownites." The EDX analysis of the plagioclases of ID 500 indicate a mean composition $An_{73}Ab_{24}Or_3$. However, these values differ from those of ID 385 it have to be noticed that the measurements were performed in low-vacuum mode without carbon coating of the sample with an acceleration voltage of 20 kV. This leads to a comparatively large interaction volume within the sample that encompasses also metallic iron phases. In addition, sodium is more difficult to detect because of its outgassing tendency. Therefore, the plagioclases are thought to contain less iron but more sodium, which in turn results in chemical compositions comparable to those of ID 385. It also verifies the findings of Irmer (1920). Velde (1920) also found two generations of plagioclases with labradortic composition using light microscopy. She also analyzed the chemical composition of one larger plagioclase inclusion and calculated $An_{55}Ab_{45}Or_0$ (Velde, 1920).

Our EMPA analysis of the ID 385 pyroxens lead to a mean composition of $En_{48}Wo_{24}Fs_{28}$. This finding is in good agreement with the findings of Velde (1920) who described the pyroxens as Mg-Diopsids and Augites based on microscopy. In addition, the pyroxen spectrum gathered at sample ID 500 is comparable to Mg-rich pyroxens (V. E. Hamilton, 2000). However, the CF of the suggested pyroxene spectrum does not fit to emission spectra of pyroxenes (e.g., V. E. Hamilton, 2000). Therefore, it is possible that the spectrum might be affected by plagioclase.

4.1. Christiansen Feature

It is known, that the CF of the plagioclases shift with An-content to longer wavelengths (Conel, 1970). However, Conel (1970) used thin films of the minerals and measured transmission and did not perform reflectance

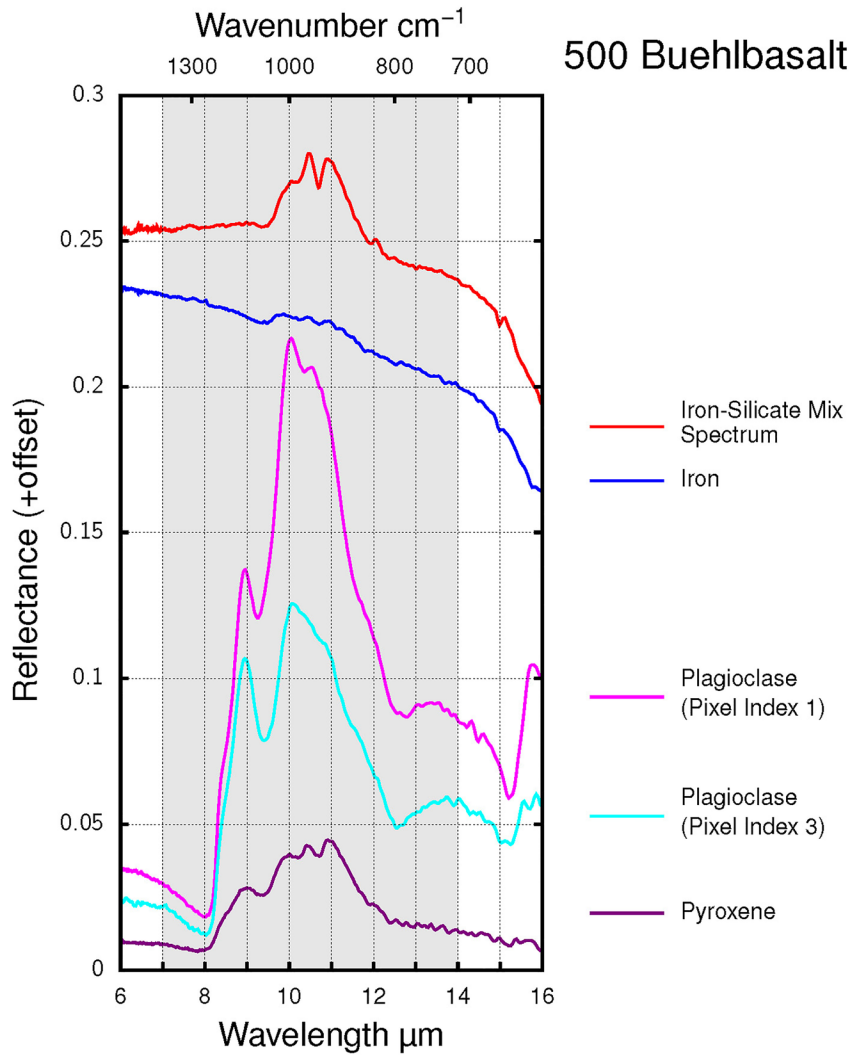

Figure 10. Spectra of ID 500. The spectrum of the pure iron is mostly featureless, measuring an area covering iron and silicate leads to superposed silicate bands on the flat iron spectrum. The spectrum of the pyroxene is noisy at the long wavelength end but the Reststrahlenbands are well-resolved.

measurements as we did in this study. In addition, the exact position of the CF can be masked by the measuring device (Salisbury & D'Aria, 1989). Therefore, the exact dependency of the CF from the An-content is possibly debatable (e.g., Reitze et al., 2021a) and depends on various factors like grain size, and environmental conditions (e.g., Donaldson Hanna et al., 2012; Shirley & Glotch, 2019). Applying the dependency of the CF from the An-content provided by Conel (1970) to feldspars described by Irmer (1920) should lead to a CF between 7.84 µm (1,276 cm^{-1}, An_{50}) to 7.92 µm (1,263 cm^{-1}, An_{70}) up to 8.01 µm (1,249 cm^{-1}, An_{90}). Most of the feldspars described by Irmer (1920) ("labradorites close to bytownites") should therefore be around the An_{70}-values and display those CF wavelength values. These values should be a first rough indication of the chemical composition and, as shown in Reitze et al. (2021b), the CFs measured with our setup are mostly comparable with the values of Conel (1970) in this specific region of chemical compositions. Nevertheless, the CFs of the feldspar spectra measured here are around 7.83 µm (ID 500) and 7.78 µm (ID 385) implying An_{45}- and An_{30}-values if we apply the study of Conel (1970). Both values indicate a more Ab-rich composition than is expected based on the earlier findings by Irmer (1920) as well as based on our microprobe analysis. However, if we fit the data from Reitze et al. (2021a) (where the grain size fraction between 63 and 125 µm was used) with a linear regression line, the expected An-contents are both An_{52} (result of the fit: $wt\%SiO_2 = 0.39 \cdot CF_{wave\#} - 434$; $R^2 = 0.97$). These An-values are consistent with our microprobe analyses of one of the measured plagioclase population. Hence, we conclude, that the dependency described by Conel (1970) needs refinement for reflectance spectra analyses

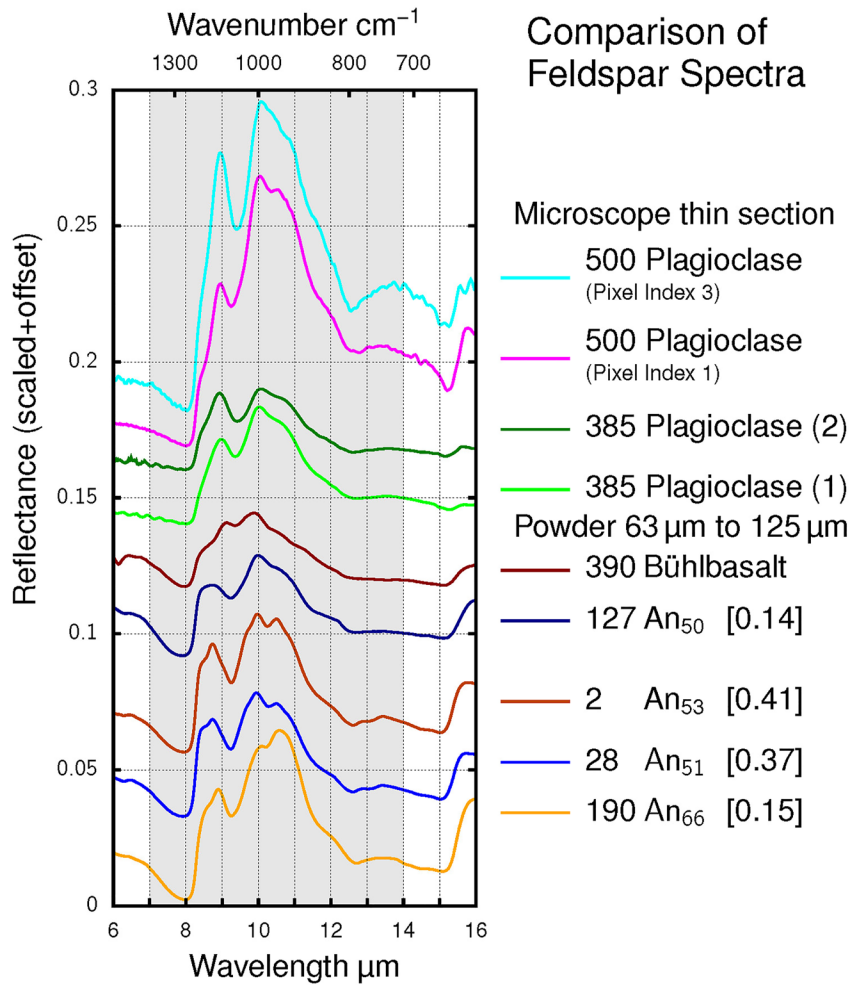

Figure 11. Comparison of feldspar spectra originating from ID 500, ID 385, the feldspar dominated bulk rock sample, ID 390, as well as well-characterized pure plagioclase samples taken from Reitze et al. (2021b). Numbers in squared brackets indicate the state of Al,Si order. Numbers in round brackets refer to the text. See text for details.

of feldspars and that the SiO_2- or An-content depends more linearly on the wavenumber of the CF at least for our two different setups, that we used.

4.2. Reststrahlen Bands

The spectral region of the RBs of silicates is dominated by vibration modes of the Si-O_4 tetrahedra (e.g., Iiishi et al., 1971). The spectra of the feldspars are also affected by the degree of Al,Si order (Reitze et al., 2020, 2021b). The wavelength region of the feldspar RBs in both samples (ID 385 and ID 500) are very similar although they crystallized under different reducing conditions. All plagioclases show an RB at around 9 µm (1,111 cm^{-1}) and another around 10 µm (1,000 cm^{-1}). In one plagioclase spectrum of ID 500 (Pixel Index 1), the RB at 10.5 µm (952 cm^{-1}) is resolved, whereas this RB is a shoulder in the other spectrum (Pixel Index 3). This is, however, not a significant difference and may be attributed to the orientation of the plagioclase crystals (e.g., Jaret et al., 2015; Ye et al., 2019). The occurrence of a strong RB around 9 µm (1,111 cm^{-1}) indicates an higher An-content than the wavelength of the CF (e.g., the plagioclase spectra of ID 500 and ID 190 in Figure 11). However, the strong RB at around 10 µm (1,000 cm^{-1}) indicates a chemical composition of the feldspar component that is expected from the wavelength of the CF (e.g., ID 500 spectra and spectra of IDs 2, 28, and 127; Figure 11). The comparison of the plagioclase spectra of ID 385 and ID 500 with the plagioclase spectra from the literature may also indicate that the ID 500 plagioclases are more ordered than the plagioclases from ID 385 (Reitze et al., 2021b). This would be the expected case, because ID 500 developed larger crystals indicating a slower cooling rate and therefore they had more time ordering the Al- and

Si-ions, which takes place always in combination with Na-Ca-diffusion (e.g., Morse, 1984). In turn, ID 385 with its small crystals is a comparatively quickly cooled effusive basalt sample in which the plagioclases cooled down faster preserving an disordered state of Al,Si order. In addition, the powdered samples ID 390 and ID 391 show similar RBs.

4.3. Sample Preparation

ID 385 consists of two areas with different color occurrence (one brighter, one darker), which were separated (ID 390 and ID 391), crushed and sieved to analyze potential spectral differences for these two areas. By applying this procedure to a sample, it must always be considered, that during crushing different mineral phases behave differently (e.g., Reitze et al., 2021a). Some phases may break up easier than others, especially minerals with a clear and good cleavage like feldspar. Furthermore, some mineral phases within the rock may be smaller than others (e.g., in a rock with a porphyritic texture). In addition, the mechanical properties of the minerals may play a role in how the minerals may separate during sample preparation. For example, assuming a rock that contains two different minerals in different amounts. Under the second assumption that these minerals have uniform or nearly uniform mechanical properties, the probability that a mineral will fracture is only a function of the amount of that mineral within the rock. Hence, the most abundant mineral will accumulate in the finer fractions. Sieving such a mixture of phases can change the modal proportions within each grain size fraction significantly. The same is true for the Moon's regolith, where the plagioclase ("feldspar"—good cleavage) component is enriched in the smallest grain size fraction (Taylor et al., 2001). In addition, the enormous thermal stress through multiple cooling and heating induced by diurnal cycles at planetary objects without atmosphere leads to the formation of flaked off particles especially of anorthositic rocks in the range between 6 and 46 µm (Patzek & Rüsch, 2022). Therefore, if remote sensing spectra of the Moon's regolith can resolve a TF, it will probably be dominated by the plagioclase component. This observation will also be true for Mercury's regolith (Reitze et al., 2021a). The enrichment of the plagioclase also have another implication: The form of the TF of the smallest grain size fraction gives a hint on the degree of Al,Si order of the feldspars (Reitze et al., 2021b). The TFs in the spectra of the <25 µm samples of ID 390 and ID 391 are sharp peaks at 12.11 µm (826 cm^{-1}) combined with a smaller peak between 11.37 µm (880 cm^{-1}) and 11.43 µm (875 cm^{-1}). This form of a double peak like TF suggests a relatively high degree of Al,Si order (Reitze et al., 2021b). In addition, the wavelength of the TF peak reflects an approx. An_{50+} composition (Reitze et al., 2021b).

Detailed deconvolution of IR spectra is challenging because the mineral components account nonlinear to the resulting bulk IR spectrum (e.g., Grumpe et al., 2018, and references therein). Grumpe et al. (2018) developed a spectral unmixing deconvolution routine that previously was successful applied to IR data taken from our database (e.g., Bauch et al., 2019; Bauch et al., 2020, 2021, 2022). However, this deconvolution algorithm have to treat not only every mineral with a specific chemical composition as one endmember, but also every grain size, and every other property which has an effect on the form of the spectra (e.g., degree of Al,Si order of feldspars (Reitze et al., 2020; Reitze et al., 2021b). Therefore, the present study is important to find out weather the redox conditions during crystallization of feldspars have an effect on the spectral information or not.

Figure 9 and Table 1 show, that the CF of the grain size fractions of ID 390 and ID 391 shift toward longer wavelengths with increasing particle size but is otherwise completely comparable between the two samples. The shift of the CF with increasing particle size is a combination of at least two factors. First, it is known that an increasing particle size leads to a shift of the CF to longer wavelengths under high vacuum (Logan et al., 1973; Shirley & Glotch, 2019). Second, the above described enrichment of the plagioclase component in the finest grain size fraction should also shift the CF to a wavelength stronger dominated by the plagioclase component. In addition, the CF may change due to environmental conditions such as sample temperature and environmental pressure (Donaldson Hanna et al., 2012). However, these factors cannot explain the shift observed because they were stable throughout our measurements. In the spectra of the larger grain sizes, we measured a CF at longer wavelength than expected for pure plagioclases with a comparable chemical composition than the feldspars within the samples. The CF in the spectra of the larger grain sizes reflect the existence of mafic minerals within the bulk sample. Mafic minerals show a CF at longer wavelength than more felsic minerals like the feldspars (e.g., Conel, 1969). Accordingly, the mafic minerals shift the CF of rock spectra to longer wavelength (e.g., Salisbury & Walter, 1989). Within the smaller grain size fractions the plagioclase component is supposed to be enriched (Reitze et al., 2021a; Taylor et al., 2001). In addition, the CF of the finer fractions of pure plagioclase spectra is shifted toward longer wavelengths under a simulated lunar environment under high vacuum (Shirley & Glotch, 2019). Therefore, the spectra of the finest fractions of ID 390 and ID 391 shift toward longer wavelength and converge to the CF that is expected for spectra of the plagioclases within the samples with a small grain size.

5. Conclusion

The mid-IR spectra of the plagioclases of ID 385 which experienced more oxidizing conditions during its crystallization than ID 500, exhibit no significant differences. Feldspars originating from both samples show CFs that are indicative for An_{52-53}. The plagioclase phases of ID 500 were measured in direct neighborhood to metallic iron. Because the formation of this iron suggests reducing conditions during the emplacement of the magma, the plagioclases around the iron likely experienced the same reducing conditions. Nevertheless, there are no spectral differences between the plagioclases of the samples ID 385 and ID 500 that need another explanation than those that can be related to differences resulting from crystal orientations, chemical compositions, grain sizes, and degrees of Al,Si order. Thus, it can be concluded, that reducing conditions during the emplacement of magmas do not affect the spectral properties of plagioclase feldspars in the mid-IR. This result is essential for the interpretation of data returned by the MERTIS instrument from Mercury, because Mercury's surface is thought to be evolved under strongly reducing conditions (Namur et al., 2016).

Data Availability Statement

All used infrared spectra are together with further information available in the MERTIS IRIS Infrared Database at http://bc-mertis-pi.uni-muenster.de/. The data can be found using the ID or the name of the sample. In the database the spectra are stored in the form "ID_Parent sample name + name label for specific mineral/phase" (example description "385_Buehlbasalt-2+Plagioclase.") If there is more than one spectrum with the same phase/mineral name for a specific sample, the spectra are sorted by measurement date and/or pixel index.

Acknowledgments
BepiColombo is a joint mission between the European Space Agency (ESA) and the Japan Aerospace Exploration Agency (JAXA) mission with contributions from its member states and partners. We acknowledge herewith the work of the whole BepiColombo team. This work is partly supported by the DLR funding 50 QW 2201A in the framework of the BepiColombo mission. We would like to thank Prof. Dr. Christian Ballhaus for providing sample with ID 500. We want to thank Ulla Heitmann for preparation of the thin sections. We would like to thank the Editor David Baratoux for approving the publication as well as the Steven Jaret and two anonymous reviewers for their helpful and constructive reviews which helped to improve the manuscript. Open Access funding enabled and organized by Projekt DEAL.

References

Anders, E. (1964). Origin, age, and composition of meteorites. *Space Science Reviews*, *3*(5–6), 583–714. https://doi.org/10.1007/bf00177954

Anser Li, Z.-X., & Aeolus Lee, C.-T. (2004). The constancy of upper mantle fo2 through time inferred from v/Sc ratios in basalts. *Earth and Planetary Science Letters*, *228*(3), 483–493. https://doi.org/10.1016/j.epsl.2004.10.006

Ballhaus, C., Leitzke, F. P., Fonseca, R. O. C., Nagel, T., Kuzmin, D., & El Goresy, A. (2022). Metal saturated cumulates from Siberia — Lunar basalt analogues? *Journal of Petrology*, *63*(8). https://doi.org/10.1093/petrology/egac067

Bauch, K. E., Hiesinger, H., Morlok, A., Reitze, M. P., Weber, I., Tiedeken, M., & Helbert, J. (2019). Deconvolution of laboratory IR spectral reflectance data for MERTIS onboard the ESA/JAXA BepiColombo mission. In *Lunar and Planetary Science Conference* (p. 2521).

Bauch, K. E., Morlok, A., Hiesinger, H., Reitze, M., Schmedemann, N., Stojic, A., et al. (2022). Unmixing of laboratory IR spectral reflectance measurements of smooth plains analogs. In *53rd Lunar and Planetary Science Conference* (Vol. 2678, p. 1989).

Bauch, K. E., Morlok, A., Hiesinger, H., Reitze, M. P., Schmedemann, N., Stojic, A. N., et al. (2021). Unmixing of laboratory IR spectral reflectance measurements of Labradorite-Enstatite-glass mineral mixtures. In *Lunar and Planetary Science Conference* (p. 1567).

Bauch, K. E., Weber, I., Reitze, M. P., Morlok, A., Hiesinger, H., Stojic, A. N., & Helbert, J. (2020). Deconvolution of laboratory IR spectral reflectance measurements of olivine and pyroxene mineral mixtures. In *Lunar and Planetary Science Conference* (p. 1523).

Benkhoff, J., Casteren, J., Hayakawa, H., Fujimoto, M., Laakso, H., Novara, M., et al. (2010). BepiColombo-Comprehensive exploration of Mercury: Mission overview and science goals. *Planetary and Space Science*, *58*(1–2), 2–20. https://doi.org/10.1016/j.pss.2009.09.020

Blanckenhorn, M., & Beyschlag, F. (1901). [Neue Nr. 4622] Wilhelmshöhe [Kassel West] / Geologische Karte. Armann & Pillmeier, Cassel http://resolver.sub.uni-goettingen.de/purl?gldocs-11858/7936

Brey, G. (1978). Origin of olivine melilitites—Chemical and experimental constraints. *Journal of Volcanology and Geothermal Research*, *3*(1), 61–88. https://doi.org/10.1016/0377-0273(78)90004-5

Conel, J. (1970). A new method for determining SiO_2 abundance in silicate glass from powder film transmission measurements. In *Space programs summary supporting research and advanced development* (Vol. iii, pp. 37–63). Jet Propulsion Laboratory.

Conel, J. E. (1969). Infrared emissivities of silicates: Experimental results and a cloudy atmosphere model of spectral emission from condensed particulate mediums. *Journal of Geophysical Research*, *74*(6), 1614–1634. https://doi.org/10.1029/JB074i006p01614

Donaldson Hanna, K. L., Sprague, A. L., Kozlowski, R. W. H., Boccafolo, K., & Warell, J. (2007). Mercury and the Moon: Initial findings from mid-infrared spectroscopic measurements of the surface. In *38th Annual Lunar and Planetary Science Conference* (p. 2291).

Donaldson Hanna, K. L., Thomas, I. R., Bowles, N. E., Greenhagen, B. T., Pieters, C. M., Mustard, J. F., et al. (2012). Laboratory emissivity measurements of the plagioclase solid solution series under varying environmental conditions. *Journal of Geophysical Research*, *117*(E11). https://doi.org/10.1029/2012je004184

El Goresy, A., Ramdohr, P., & Taylor, L. A. (1971). The opaque minerals in the lunar rocks from Oceanus Procellarum. *Lunar and Planetary Science Conference Proceedings*, *2*, 219.

Grumpe, A., Mengewein, N., Rommel, D., Mall, U., & Wöhler, C. (2018). Interpreting spectral unmixing coefficients: From spectral weights to mass fractions. *Icarus*, *299*, 1–14. https://doi.org/10.1016/j.icarus.2017.07.008

Hamilton, D. L., Burnham, C. W., & Osborn, E. F. (1964). The solubility of water and effects of oxygen fugacity and water content on crystallization in Mafic Magmas. *Journal of Petrology*, *5*(1), 21–39. https://doi.org/10.1093/petrology/5.1.21

Hamilton, V. E. (2000). Thermal infrared emission spectroscopy of the pyroxen mineral series. *Journal of Geophysical Research*, *105*(E4), 9701–9716. https://doi.org/10.1029/1999je001112

Hapke, B., & Sato, H. (2016). The porosity of the upper lunar regolith. *Icarus*, *273*, 75–83. https://doi.org/10.1016/j.icarus.2015.10.031

Hiesinger, H., Helbert, J., Alemanno, G., Bauch, K. E., D'Amore, M., Maturilli, A., et al. (2020). Studying the composition and mineralogy of the Hermean surface with the Mercury Radiometer and Thermal Infrared Spectrometer (MERTIS) for the BepiColombo mission: An update. *Space Science Reviews*, *216*(6), 110. https://doi.org/10.1007/s11214-020-00732-4

Hiesinger, H., Helbert, J., Bauch, K., D'Amore, M., Maturilli, M., Morlok, A., et al. (2021). The Mercury Radiometer and Thermal Infrared Spectrometer (MERTIS) at the Moon—First results and status report. In *52nd Lunar and Planetary Science Conference* (p. 1494).

Hiesinger, H., Helbert, J., & MERTIS Co-I Team (2010). The Mercury Radiometer and Thermal Infrared Spectrometer (MERTIS) for the Bepi-Colombo mission. *Planetary and Space Science*, *58*(1–2), 144–165. https://doi.org/10.1016/j.pss.2008.09.019

Hornstein, F. F. (1907). Mitteilung über das Vorkommen von makroskopischen Einschlüssen gediegenen Eisens in Basalt aus der Gegend von Cassel. In *Centralblatt für Mineralogie, Geologie und Paläontologie* (pp. 276–279).

Iacono-Marziano, G., Gaillard, F., Scaillet, B., Polozov, A. G., Marecal, V., Pirre, M., & Arndt, N. T. (2012). Extremely reducing conditions reached during basaltic intrusion in organic matter-bearing sediments. *Earth and Planetary Science Letters*, *357–358*, 319–326. https://doi.org/10.1016/j.epsl.2012.09.052

Iiishi, K., Tomisaka, T., Kato, T., & Umegaki, Y. (1971). Isomorphous substitution and infrared and far infrared spectra of the feldspar group. *N Jb Miner Abh*, *115*, 98–119.

Irmer, W. (1920). Das Vorkommen tellurischen Eisens im Basalte des Bühls bei Kassel, seine Begleitmineralien und Genesis. Der Basalt des Bühls bei Kassel und seine Einschlüsse von Magnetit, Magnetkies und gediegenem Eisen. *Abhandlungen der Senckenbergischen Naturforschenden Gesellschaft*, *37*(2), 83–108.

Jaret, S. J., Woerner, W. R., Phillips, B. L., Ehm, L., Nekvasil, H., Wright, S. P., & Glotch, T. D. (2015). Maskelynite formation via solid-state transformation: Evidence of infrared and X-ray anisotropy. *Journal of Geophysical Research: Planets*, *120*(3), 570–587. https://doi.org/10.1002/2014JE004764

Karl, H.-V. (2021). Die Wirbeltiere aus dem Niederhessischen Braunkohlenrevier um Borken, unter besonderer Berücksichtigung der Schildkröten- und Krokodilreste mit taxonomischen Notizen zu Geoemyda saxonica Hummel, 1935 (Hessen, Deutschland). *Mainzer natruwiss Archiv*, *57*, 101–132.

Kokaly, R., Clark, R., Swayze, G., Livo, K., Hoefen, T., Pearson, N., et al. (2017). *USGS Spectral Library Version 7 Data* (Vol. 1035, p. 61). US Geological Survey Data Series. https://doi.org/10.3133/ds1035

Kortüm, G. (1969). Reguläre und diffuse reflexion. In *Reflexionsspektroskopie: Grundlagen, methodik, anwendungen* (pp. 5–73). Springer Berlin Heidelberg. https://doi.org/10.1007/978-3-662-29788-9_2

Köster, H. (1953). Molybdänglanzkristall aus dem Basalt des Bühls bei Kassel. *Heidelberger Beiträge zur Mineralogie und Petrographie*, *3*(5), 406–408. https://doi.org/10.1007/bf01141465

Logan, L. M., Hunt, G. R., Salisbury, J. W., & Balsamo, S. R. (1973). Compositional implications of christiansen frequency maximums for infrared remote sensing applications. *Journal of Geophysical Research*, *78*(23), 4983–5003. https://doi.org/10.1029/JB078i023p04983

Lyon, R. (1964). Evaluation of infrared spectrometry for compositional analysis of lunar and planetary soils partii: Rough and powdered surfaces. NASA Rept. CR-100.

McCubbin, F. M., Vander Kaaden, K. E., Peplowski, P. N., Bell, A. S., Nittler, L. R., Boyce, J. W., et al. (2017). A low o/si ratio on the surface of mercury: Evidence for silicon smelting? *J Geophys Res Planet*, *122*(10), 2053–2076. https://doi.org/10.1002/2017JE005367

Medenbach, O., & El Goresy, A. (1982). Ulvöspinel in native iron-bearing assemblages and the origin of these assemblages in basalts from Ovifak, Greenland, and Bühl, Federal Republic of Germany. *Contributions to Mineralogy and Petrology*, *80*(4), 358–366. https://doi.org/10.1007/BF00378008

Möhl, H. (1868). Der Bühl bei Weimar in der Nähe von Kassel. Beitrag zur vulkanischen Entstehung basaltischer Gesteine. In *Neunter Bericht des Offenbacher Vereins für Naturkunde über seine Thätigkeit* (pp. 61–80).

Morlok, A., Renggli, C., Charlier, B., Reitze, M. P., Klemme, S., Namur, O., et al. (2021). Mid-infrared reflectance spectroscopy of synthetic glass analogs for mercury surface studies. *Icarus*, *361*, 114363. https://doi.org/10.1016/j.icarus.2021.114363

Morse, S. A. (1984). Cation diffusion in plagioclase feldspar. *Science*, *225*(4661), 504–505. https://doi.org/10.1126/science.225.4661.504

Namur, O., & Charlier, B. (2017). Silicate mineralogy at the surface of Mercury. *Nature Geoscience*, *10*(1), 9–13. https://doi.org/10.1038/ngeo2860

Namur, O., Charlier, B., Holtz, F., Cartier, C., & McCammon, C. (2016). Sulfur solubility in reduced mafic silicate melts: Implications for the speciation and distribution of sulfur on mercury. *Earth and Planetary Science Letters*, *448*, 102–114. https://doi.org/10.1016/j.epsl.2016.05.024

Paige, D. A., Foote, M. C., Greenhagen, B. T., Schofield, J. T., Calcutt, S., Vasavada, A. R., et al. (2010). The Lunar Reconnaissance Orbiter Diviner Lunar Radiometer Experiment. *Space Science Reviews*, *150*(1–4), 125–160. https://doi.org/10.1007/s11214-009-9529-2

Papike, J., Karner, J., & Shearer, C. (2004). Comparative planetary mineralogy: V/(Cr + Al) systematics in chromite as an indicator of relative oxygen fugacity. *American Mineralogist*, *89*(10), 1557–1560. https://doi.org/10.2138/am-2004-1027

Patzek, M., & Rüsch, O. (2022). Experimentally induced thermal fatigue on lunar and eucrite meteorites—Influence of the mineralogy on rock breakdown. *Journal of Geophysical Research: Planets*, *127*(10), e2022JE007306. https://doi.org/10.1029/2022JE007306

Pernet-Fisher, J. F., Day, J. M., Howarth, G. H., Ryabov, V. V., & Taylor, L. A. (2017). Atmospheric outgassing and native-iron formation during carbonaceous sediment–basalt melt interactions. *Earth and Planetary Science Letters*, *460*, 201–212. https://doi.org/10.1016/j.epsl.2016.12.022

Pieters, C. M. & Englert, P. A. J. (Eds.) (1993). *Remote geochemical analysis: Elemental and mineralogical composition. Topics in remote sensing 4*. Cambridge University Press.

Ramdohr, P. (1953). *Maldonit: Neue beobachtungen am bühl-eisen*. Akad.-Verlag.

Reitze, M. P., Weber, I., Kroll, H., Morlok, A., Hiesinger, H., & Helbert, J. (2020). Mid-infrared spectroscopy of alkali feldspar samples for space application. *Mineralogy and Petrology*, *114*(5), 453–463. https://doi.org/10.1007/s00710-020-00709-9

Reitze, M. P., Weber, I., Morlok, A., Hiesinger, H., Bauch, K. E., Stojic, A. N., & Helbert, J. (2021a). Mid-infrared spectroscopy of anorthosite samples from near manicouagan crater, Canada, as analogue for remote sensing of mercury and other terrestrial solar system objects. *Journal of Geophysical Research: Planets*, *126*, e2021JE006832. https://doi.org/10.1029/2021JE006832

Reitze, M. P., Weber, I., Morlok, A., Hiesinger, H., Bauch, K. E., Stojic, A. N., & Helbert, J. (2021b). Mid-infrared spectroscopy of crystalline plagioclase feldspar samples with various Al, Si order and implications for remote sensing of Mercury and other terrestrial Solar System objects. *Earth and Planetary Science Letters*, *554*, 116697. https://doi.org/10.1016/j.epsl.2020.116697

Ryabov, V., & Lapkovsky, A. (2010). Native iron (–platinum) ores from the Siberian platform trap intrusions. *Australian Journal of Earth Sciences*, *57*(6), 707–736. https://doi.org/10.1080/08120091003739056

Salisbury, J. W., & D'Aria, D. M. (1989). Measurement of Christiansen frequencies in spectra of particulate samples for determination of rock composition. *Abstracts of the Lunar and Planetary Science Conference*, *20*, 940.

Salisbury, J. W., & Eastes, J. W. (1985). The effect of particle size and porosity on spectral contrast in the mid-infrared. *Icarus*, *64*(3), 586–588. https://doi.org/10.1016/0019-1035(85)90078-8

Salisbury, J. W., & Wald, A. (1992). The role of volume scattering in reducing spectral contrast of Reststrahlen bands in spectra of powdered minerals. *Icarus*, *96*(1), 121–128. https://doi.org/10.1016/0019-1035(92)90009-V

Salisbury, J. W., & Walter, L. S. (1989). Thermal infrared (2.5-13.5 μm) spectroscopic remote sensing of igneous rock types on particulate planetary surfaces. *Journal of Geophysical Research: Solid Earth*, *94*(B7), 9192. https://doi.org/10.1029/jb094ib07p09192

Shirley, K. A., & Glotch, T. D. (2019). Particle size effects on mid-infrared spectra of lunar analog minerals in a simulated lunar environment. *J Geophys Res: Planet*, *124*(4), 970–988. https://doi.org/10.1029/2018JE005533

Sprague, A. L., Donaldson Hanna, K. L., Kozlowski, R. W. H., Helbert, J., Maturilli, A., Warell, J. B., & Hora, J. L. (2009). Spectral emissivity measurements of Mercury's surface indicate Mg- and Ca-rich mineralogy, K-spar, Na-rich plagioclase, rutile, with possible perovskite, and garnet. *Planetary and Space Science*, *57*(3), 364–383. https://doi.org/10.1016/j.pss.2009.01.006

Sprague, A. L., Emery, J. P., Donaldson, K. L., Russell, R. W., Lynch, D. K., & Mazuk, A. L. (2002). Mercury: Mid-infrared (3–13.5 μm) observations show heterogeneous composition, presence of intermediate and basic soil types, and pyroxene. *Meteoritics & Planetary Science*, *37*(9), 1255–1268. https://doi.org/10.1111/j.1945-5100.2002.tb00894.x

Sprague, A. L., Kozlowski, R. W. H., Witteborn, F. C., Cruikshank, D. P., & Wooden, D. H. (1994). Mercury: Evidence for Anorthosite and Basalt from mid-infrared (7.3-13.5 μm) spectroscopy. *Icarus*, *109*(1), 156–167. https://doi.org/10.1006/icar.1994.1083

Sprague, A. L., Nash, D. B., Witteborn, F., & Cruikshank, D. P. (1997). Mercury's feldspar connection - mid-IR measurements suggest plagioclase. *Advances in Space Research*, *19*(10), 1507–1510. https://doi.org/10.1016/s0273-1177(97)00363-3

Sprague, A. L., Warell, J., Cremonese, G., Langevin, Y., Helbert, J., Wurz, P., et al. (2007). Mercury's surface composition and character as measured by ground-based observations. *Space Science Reviews*, *132*(2–4), 399–431. https://doi.org/10.1007/s11214-007-9221-3

Stojic, A. N., Morlok, A., Tollan, P., Kohout, T., Hermann, J., Weber, I., et al. (2021). A shock recovery experiment and its implications for mercury's surface: The effect of high pressure on porous olivine powder as a regolith analog. *Icarus*, *357*, 114162. https://doi.org/10.1016/j.icarus.2020.114162

Taylor, L. A., Pieters, C. M., Keller, L. P., Morris, R. V., & McKay, D. S. (2001). Lunar mare soils: Space weathering and the major effects of surface-correlated nanophase fe. *Journal of Geophysical Research: Planet*, *106*(E11), 27985–27999. https://doi.org/10.1029/2000JE001402

Velde, L. (1920). Das Vorkommen tellurischen Eisens im Basalte des Bühls bei Kassel, seine Begleitmineralien und Genesis. Die silikatisehen Einschlüsse im Basalte des Bühls. *Abhandlungen der Senckenbergischen Naturforschenden Gesellschaft*, *37*(2), 109–136.

Weber, I., Morlok, A., Grund, T., Bauch, K. E., Hiesinger, H., Stojic, A., et al. (2018). A mid-infrared reflectance database in preparation for space missions. In *Lunar and Planetary Science Conference* (p. 1430).

Weber, I., Stojic, A. N., Morlok, A., Reitze, M. P., Markus, K., Hiesinger, H., et al. (2020). Space weathering by simulated micrometeorite bombardment on natural olivine and pyroxene: A coordinated IR and TEM study. *Earth and Planetary Science Letters*, *530*, 115884. https://doi.org/10.1016/j.epsl.2019.115884

Ye, C., Rucks, M. J., Arnold, J. A., & Glotch, T. D. (2019). Mid-infrared optical constants of labradorite, a triclinic plagioclase mineral. *Earth and Space Science*, *6*(12), 2410–2422. https://doi.org/10.1029/2019EA000915